PHYSICAL REVIEW B **91**, 115315 (2015)

Intrinsic origin of two-dimensional electron gas at the (001) surface of $SrTiO_3$

Pietro Delugas,[1] Vincenzo Fiorentini,[2] Alessandro Mattoni,[3] and Alessio Filippetti[3]
[1]*Istituto Italiano di Tecnologia - IIT, Via Morego 30, I-16163 Genova, Italy*
[2]*Dipartimento di Fisica and CNR-IOM, Università di Cagliari, S.P. Monserrato-Sestu Km. 0.700, I-Monserrato (CA), Italy*
[3]*CNR-IOM, UOS Cagliari, c/o Dipartimento di Fisica, Università di Cagliari, S.P. Monserrato-Sestu Km. 0.700, I-Monserrato CA, Italy*

(Received 7 November 2014; revised manuscript received 12 March 2015; published 26 March 2015)

It is generally assumed that two-dimensional electron gas (2DEG) recently observed at the (001) $SrTiO_3$ surface can be solely derived by oxygen vacancies introduced during ultrahigh vacuum annealing or through ultraviolet irradiation exposure. However, 2DEG entirely due to defect formation may be at odds with the characteristics of high mobility and easy field-effect manipulation required for applications; to that aim, an intrinsic formation mechanism should be preferred. Using advanced *ab initio* simulations we give evidence that 2DEG at the (001) $SrTiO_3$ surface may even result from purely intrinsic properties of the pristine surface, provided that the surface is SrO terminated. The key concept is that the SrO termination is electron-attractive as a consequence of both the surface-induced polarity and the specific electronic reconstruction, whereas the TiO_2 termination is electron-repulsive. It follows that in vacuum-cleaved samples where both terminations are present, 2DEG can result from the structurally ordered superposition of the two kinds of domain, even in the absence of any extrinsic source. On the other hand, in etching-prepared single-terminated TiO_2 samples 2DEG should be assumed as entirely derived by extrinsic factors.

DOI: 10.1103/PhysRevB.91.115315 PACS number(s): 73.20.At, 73.40.Lq, 73.50.Lw, 73.63.Hs

I. INTRODUCTION

The discovery by Ohtomoand Hwang of two-dimensional electron gas (2DEG) at the $SrTiO_3/LaAlO_3$ (STO/LAO) interface has stimulated an intensive search of 2DEG in a vast range of oxide systems, lured by the appealing perspective that charge confinement could be a common occurrence in oxide heterostructure. Alas, despite the huge effort accomplished, very few certified cases of 2DEG observations can be claimed so far. The most surprising is perhaps the (001) surface of $SrTiO_3$ (STO): Several angle-resolved photoelectron emission (ARPES) measurements [1–5] have recently revealed the presence of 2DEG at the surface. This is an astonishing result, obtained after decades of intensive attempts to induce metallization in STO surfaces by a number of different strategies (from Ar+ bombardment [6] to H adsorption [7], electron-beam evaporation [8], and field effect [9]).

It is important to notice that while some noticeable differences among the various ARPES experiments emerge (indicating that specific samples and experimental setting should not be overlooked), they all substantially agree on some key features, primarily the presence of one or more broad bands, downshifted by ~0.2–0.1 eV from the Fermi energy (E_F), with Fermi vector (K_F) $\simeq$ 0.1–0.2 Å^{-1}, and closely reminiscent of the $3d$ d_{xy} bands hosting most of the 2DEG charge at the STO/LAO interface; flatter signals to be attributed to d_{xz}, d_{yz} bands are also present in most of these spectra.

While the observations are indisputable, less obvious is the interpretation. All the ARPES measurements seem to coherently exclude the occurrence of an atomic reconstruction. In Ref. [1] n doping is caused by oxygen vacancies introduced by growth under low-oxygen pressure, and it is speculated that upon cleavage a large fraction of vacancies could migrate to the surface, providing the binding energy responsible for the gas confinement. Remarkably, samples with very different three-dimensional (3D) doping concentrations exhibit substantially similar surface spectra, suggesting a scenario where 2DEG (dubbed *universal* in Ref. [1]) is largely independent of the bulk doping regime. In Ref. [2] stable 2DEG is induced by exposing the surface to synchrotron ultraviolet light irradiation. Amazingly, the irradiation dose is used to control 2DEG charge density: By increasing the dose, the ARPES signal is progressively enhanced, and shows deeper bands and larger Fermi surface areas. Here authors speculate that 2DEG may originate from surface oxygen deficiency caused by light-induced oxygen desorption from the surface. Finally, in Ref. [3] a highly TiO_2-terminated surface was prepared by chemical etching under high oxidation, and then annealed *in situ* in ultrahigh vacuum (UHV) to induce oxygen vacancies. Interestingly, here it is found that the change during UHV irradiation in the spectral weight of the valence bands is not simply proportional to a change in the oxygen content, i.e., irradiation can induce not just a mere n doping, but nontrivial changes in the electronic structure as well. Two-dimensional electron gas at the TiO_2-terminated surface can be also induced by UHV annealing at low temperature, as revealed by scanning-tunneling spectroscopy [10].

While it is certainly reasonable that oxygen vacancies play an important (perhaps dominant) role in the chemistry of the STO surface, the idea that 2DEG may be solely due to oxygen vacancies is somewhat disturbing, especially because the large sheet carrier density deduced in the ARPES experiments (up to $n_{2D} \sim 10^{14}$ cm^{-2}) implies similarly large vacancy concentrations, clearly at odds with the idea of a highly mobile surface 2DEG. In this work we analyze the pristine STO surface in the absence of oxygen vacancies and irrespective of any perturbing effect that a strong ultraviolet irradiation may cause to the system. We give evidence that in fact the two-dimensional (2D) confinement can even occur on the basis of the intrinsic properties of the (001) STO surface, but only for the SrO termination; 2DEG with n_{2D} as large as 6×10^{13} $electrons/cm^2$ is formed on the pristine surface without the need for invoking structural defects or reconstructions. Eventually, oxygen vacancies piling up at the surface will further enhance the sheet density and the charge confinement, as discussed on the basis of simple electrostatic modeling in Ref. [1].

A very crucial aspect which emerges from our results, and is somewhat overlooked in previous literature, is that the two unreconstructed (001) terminations (TiO_2 and SrO) have crucially different electronic structure. Since they are both thermodynamically stable and have comparable surface energy [11,12], it is normally assumed that the as-received single-crystal vacuum-cleaved STO (001) surface exposes to the vacuum both terminations, usually in the form of large, flat terraces of submicron size separated by steps of half-unit cell height [13–15]. If the terraces are large enough to recover the local properties of the (1×1) surface but smaller than the light spot size, then the observed photoemission spectra will display features derived from a superposition of the two terminations. While ARPES cannot establish a connection between measured bands and a specific termination, this can be efficiently done by *ab initio* computations, provided that an advanced methodology is used to accurately reproduce the electronic structure of the oxides (see Method section). Our calculations unveil the fundamental characteristics of the intrinsic surface: At the SrO-termination the surface-induced polarity attracts the electrons into surface bands with large k dispersion in the surface-parallel plane, favoring the formation of 2DEG similar to that found at the STO/LAO interface. The TiO_2-terminated surface, on the other hand, is unfavorable to 2D confinement; thus, n doping may result in a charge density spread through the substrate in 3D fashion, rather than tightly confined at the surface. The juxtaposition of the band energies calculated for the two types of terminations reproduces many of the ARPES features reported for the as-cleaved surface in Refs. [1] and [2]. On the other hand, for chemical-etched TiO_2 terminated surfaces, the first ARPES data [16] could not reveal 2DEG, probably as a consequence of the high annealing temperature. In fact, the very recent results of Ref. [3] show that 2DEG also appears at the etched-prepared TiO_2-terminated surface, upon UHV annealing and irradiation.

II. METHODS

Structural and electronic properties of the STO surface are calculated by first principles using the variational pseudoself interaction correction (VPSIC) approach [17] which was shown to be very accurate in the description of STO/LAO [18,19] and a variety of other oxide heterostructures [20–23]. For the VPSIC calculation the PWSIC code is used, implemented in plane waves plus the ultrasoft pseudopotentials basis set. All self-consistent calculations are run with a 35-Ryd cutoff energy and a $8\times8\times1$ k-point mesh in Fourier space. The electronic structure used for DOS and transport properties are calculated on a $24\times24\times1$ k-point mesh, further interpolated on very dense grids by the linear tetrahedron method. The two surface terminations are simulated using distinct symmetric supercells with 14.5 STO unit cells along the surface-orthogonal (c) axis, and a vacuum region corresponding to 2.5 STO units (it was checked that this vacuum is sufficient to disentangle the two surfaces). The macroscopic average of the electrostatic potential is calculated following the procedure introduced by Baldereschi *et al.* [24,25]: The electrostatic potential is averaged in the surface-orthogonal direction over a $[z-c/2, z+c/2]$ segment at any z, if c is the unit cell size. This represents a uniquely defined procedure to separate bulklike and surface regions of the supercell.

In our calculations n-type doping is treated as in the following: At any doping concentration a corresponding fraction of electron charge is added into the supercell and the self-consistent calculation rerun with this charge. In this way the rigid band approximation, typically inaccurate for oxide heterostructures, is avoided. This procedure is operatively analogous to charge control by field effect, or to low-concentration chemical doping, i.e., doping whose point-charge density is not large enough to significantly affect the pristine system. In other words, the method captures the effects of conduction charge at a purely intrinsic level, while the confining effect due to a concentration of oxygen vacancies near the surface is not included (we notice that actual oxygen vacancy simulations at reasonably low concentration would require a computing effort which largely overcomes present *ab initio* computing capabilities). This doping treatment was previously applied to other oxides [19,22] with satisfying results.

The VPSIC-calculated electronic energies $\epsilon_{n\mathbf{k}}$ are used as input for the calculation of electric transport properties through the Bloch-Boltzmann theory (BBT) in relaxation time approximation [26], as implemented in the BOLTZTRAP code [27]. The dc conductivity σ_j (here j is a component parallel to the surface) is calculated as a sum of individual band conductivities σ_{nj}. In BBT,

$$\sigma_{nj} = \frac{e^2}{V}\int d\mathbf{k}\,\tau_{n\mathbf{k}}\left(-\frac{\partial f}{\partial\epsilon_{n\mathbf{k}}}\right)v_{n\mathbf{k},j}^2, \tag{1}$$

where V is the volume, $f(\epsilon_{n\mathbf{k}})$ the Fermi occupancy, $\tau_{n\mathbf{k}}$ the relaxation time, and $v_{n\mathbf{k},j}$ the Fermi velocity. Assuming $\tau_{n\mathbf{k}} = \tau(\epsilon_{n\mathbf{k}})$, the integral in Eq. (1) can be transformed in a simpler one-dimensional (1D) integral over energy. Since the usual assumption of a constant relaxation time is insufficient for a quantitative comparison with experiment, we use analytical models to express $\tau_{n\mathbf{k}}$ in energy-dependent and temperature-dependent form. The model includes contributions from acoustic-phonon scattering (AP) and impurity scattering (IS), which are the most important at low T, and polar optical-phonon scattering (POS), which is known to be dominant for STO at room T. AP is treated within the elastic deformation potential approach (hereafter the electron energy is always relative to the CBB):

$$\tau_{\mathrm{AP}}^{-1}(T,\epsilon) = \frac{(2\tilde{m})^{\frac{3}{2}}K_B T D^2\epsilon^2}{2\pi\hbar^4\rho v_S^2}, \tag{2}$$

where D is the deformation potential, ρ the mass density, v_S the sound velocity, and $\tilde{m}$ the average effective mass in the plane. For IS the well-known Brooks-Herring formula is adopted:

$$\tau_{\mathrm{IS}}^{-1}(T,\epsilon) = \frac{\pi n_I Z_I^2 e^4\epsilon^{-3/2}}{\sqrt{2\tilde{m}}(4\pi\kappa_0\kappa)^2} \times\left[\log\left(1+\frac{8\tilde{m}\epsilon}{\hbar^2 q_0^2}\right) - \frac{1}{1+(\hbar^2 q_0^2/8\tilde{m}\epsilon)}\right], \tag{3}$$

where n_I is the impurity concentration, Z_I the impurity charge, κ_0 and κ the vacuum permittivity and the relative dielectric constant, and $q_0 = \sqrt{e^2 n_I/(\kappa_0 \kappa K_B T)}$ the Debye screening length. Finally the POS is modeled according to a simplified approach described by Ridley (see [28] and references therein) which was shown to be accurate for doped wide-gap insulators [29]. For a relevant longitudinal optical phonon energy $\hbar\omega_{\mathrm{LO}}$, the associated relaxation time is, for $\epsilon < \hbar\omega_{\mathrm{LO}}$,

$$\tau_{\mathrm{POS}}(T,\epsilon) = \frac{Z\epsilon^{3/2}}{C(T,\epsilon)}, \tag{4}$$

also called "standard" expression, and for $\epsilon > \hbar\omega_{\mathrm{LO}}$,

$$\tau_{\mathrm{POS}}(T,\epsilon) = \frac{Z\epsilon^{3/2}}{C(T,\epsilon) - A(T,\epsilon) - B(T,\epsilon)}, \tag{5}$$

known as "drift" expression (the values of A, B, C, and Z which depend on $\hbar\omega_{\mathrm{LO}}$ can be found in Ridley's article [28]). While the standard expression is quite accurate for $\epsilon < \hbar\omega_{\mathrm{LO}}$, the drift becomes exact in the limit of large electron energies. Since for STO there are three dominant longitudinal optical phonons at 21, 58, and 99 meV [30], they are treated as individual scatterers, and for each of them the relaxation time is calculated according to (4) and (5) and then summed according to Matthiessen's rule. For the parameters entering the relaxation time expressions, it is reasonable to adopt values appropriate for STO bulk: $v_S = 7.9\times10^5$ cm/s, $\kappa = 300$, $D = 15$ eV, $\epsilon_\infty = 5.2$, $\tilde{m} = 1.2\, m_e$.

III. RESULTS

A. Structure

The (1×1) surface is known to be stable under typical pressure, temperature, and chemical growing conditions. A variety of structural reconstructions was also reported for certain growth techniques and processing [31–38]. However, since reconstructions are apparently excluded in the ARPES experiments which represent our main target here, we can limit our study to the (1×1).

The (1×1) STO surface was extensively investigated by a number of experimental techniques, including surface x-ray diffraction (XRD) [34,35,39–42], low-energy electron diffraction (LEED) [13], reflection high-energy electron diffraction (RHEED) [15,39,43,44], and medium energy ion scattering (MEIS) [45–47]. A long list of theoretical works [11,12,48–54] mainly based on various *ab initio* methods, is also present in literature. And yet, despite this remarkable amount of work, there is not a clear, univocal understanding concerning the behavior of the atomic relaxations at this surface. For *ab initio* calculations, specific relaxation amplitudes may be subtly dependent on the specific energy functional employed as a reflex of the actual complexity of this surface. However, the most important qualitative trends are coherently reproduced in the majority of the cases. An unbiased comparison with the experiments, on the other hand, is made extremely difficult by a number of factors: Vacuum-cleaved samples often present a surface combining both terminations, which are not easily disentangled; also, oxygen vacancies introduced along with UHV annealing or chemical etching, disorder, corrugation, and molecular contaminants, are all ingredients which can set apart the observations from the theoretical results for the ideal, single-terminated surface.

The calculated structure of the unreconstructed (1×1) TiO_2 and SrO terminations is reported in Figs. 1(a) and 1(b), respectively. Atomic relaxations, in the percentage of the lattice parameter a_0 (we fixed $a_0 = 3.863$ Å, that is, the theoretical value for the cubic phase) are reported in Table I. Comparing our results with previous calculations (see, e.g., Ref. [49] where a large collection of results obtained by a number of *ab initio* and core-shell methods is listed), we see that the most important behaviors are consistently described: (i) For both terminations, the surface effects are rather short ranged. Relaxations are largest at the surface layer, and fade away completely going four or five monolayers away from the surface; (ii) for both terminations the largest displacement is that of the surface cations, which move inward by an amount of about 6% for SrO and 5% for TiO_2 termination, respectively; (iii) the subsurface cation movement is opposite in sign to (and smaller in amplitude than) that of the surface cation; this sign alternation of the cations continues also in the third and fourth monolayer below the surface, and is coherently described by the vast majority of previous calculations; (iv) oxygens move by a much smaller extent than cations (at most by less than 2%, according to our results). For the SrO termination the oxygen movement is always outward, while for TiO_2 may be either outward or inward.

Table I also reports the change in the distance (Δd_{12}) between surface and subsurface layer in units of a_0 for SrO and TiO_2 terminations, respectively. We found a contraction by 4.9% and 4.3% for SrO and TiO_2 terminations, respectively, in the range of previous theoretical calculations [54]. These contractions are in striking discrepancy with the outward surface relaxation observed in most of the LEED and RHEED experiments for both terminations; for example, RHEED [43,44] gives $\Delta d_{12} = +2.6\%$ and $+1.8\%$ for SrO and TiO_2, respectively; however, we should consider that in LEED and RHEED a depth-resolved reconstruction of surface relaxations is extremely difficult due to multiple electron scattering, in particular for oxides. Concerning XRD, which should be the most accurate approach to the determination of surface relaxations, Ref. [42] analyzes chemically etched, TiO_2-terminated surfaces, reporting displacements for Ti and Sr whose sign and amplitude are sensitively dependent on the specific sample, while Ref. [34] report surprisingly large (up to 20%) outward relaxations for the surface Ti at the etched TiO_2 termination. Clearly, a univocally accepted experimental determination of the actual structure of the STO surface is still lacking.

A key aspect of the STO surface is the surface-induced electric polarization, previously discussed in several experimental [13,34] and theoretical works [11,12,55]. Since (001) planes are all neutral, their rigid mutual displacements do not cause any polar deformation; however, a local polarization arises due to the oxygen-cation relative displacement along the z axis (rumpling). Our calculated rumpling values for the surface layer of the two terminations (reported in Table I) are in good agreement with the values -4.1 and -2.6 for SrO and TiO_2, respectively, obtained by LEED [13] and RHEED [43,44], and in line with previous calculations (see,

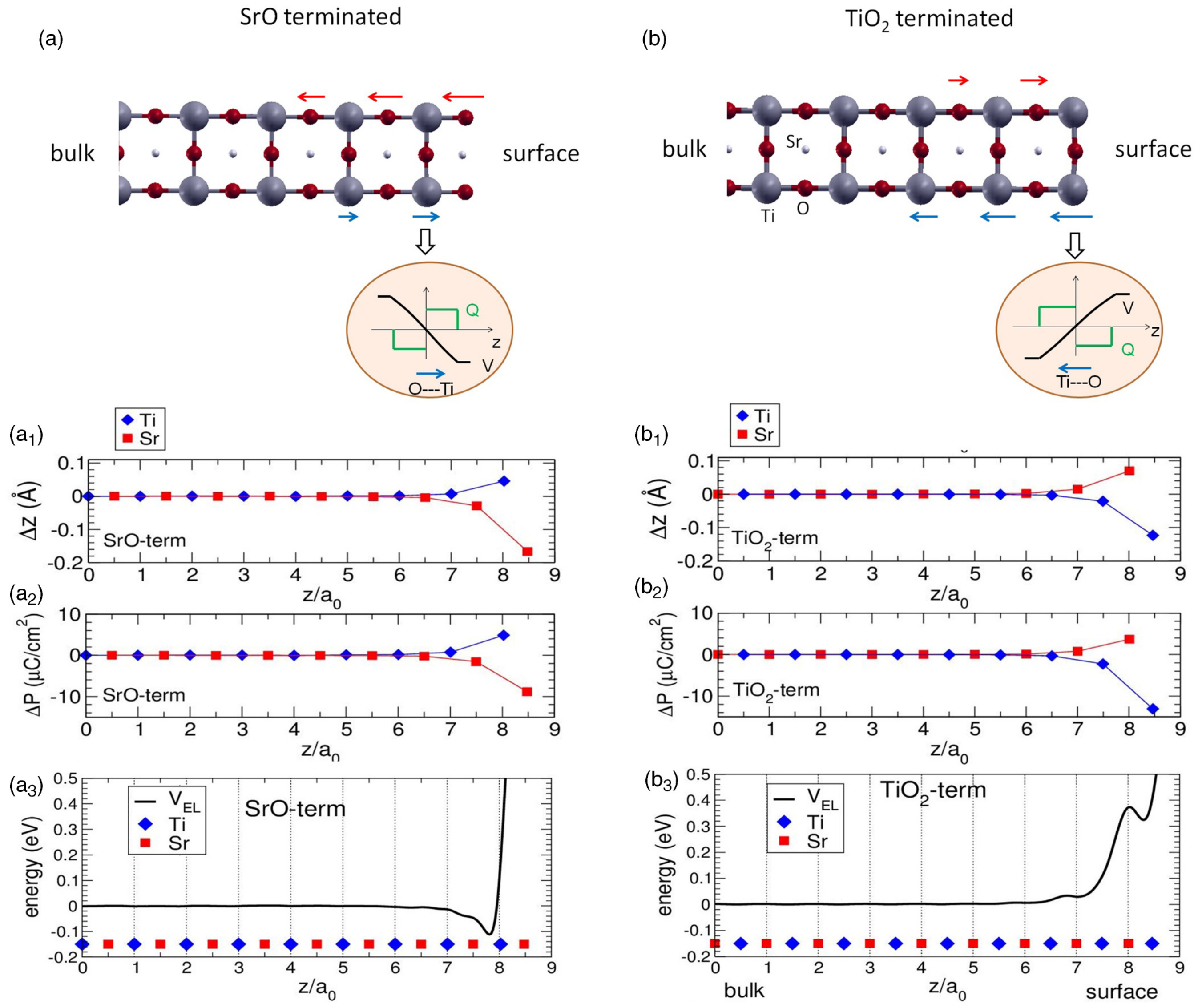

FIG. 1. (Color online) (a) and (b) Calculated structure of the two (1×1) surface terminations. Arrows indicate the direction of the Ti-O (blue) and Sr-O (red) off-plane shift (dipole) along the z axis, with arrow lengths roughly proportional to the displacement amplitudes. Insets show a cartoon of the charge dipole Q (green curves) and the corresponding electrostatic potential V (black) seen by the electrons at the most external TiO$_2$ layer of each termination: For SrO, the dipole potential pushes the electrons towards the surface; for TiO$_2$, electrons are repelled from the surface; (a$_1$) plane-by-plane cation-oxygen off-plane displacements for the SrO termination (blue diamonds are for Ti-O, red squares for Sr-O). (a$_2$) Corresponding electric dipoles for each monolayer ΔP. (a$_3$) Macroscopic-averaged electrostatic potential seen by the electrons. All quantities are plotted vs the z axis orthogonal to the surface, as a function of relative cation position z/a_0 ($z/a_0 = 0$ is for the inmost layer, $z/a_0 \sim 8.5$ for the surface layer). (b$_1$) is the same as (a$_1$) for the TiO$_2$ termination.

e.g., Ref. [48] for a comparison of rumpling values calculated with different methods).

In Figs. 1(a$_1$) and 1(b$_1$), we report the layer-by-layer rumpling calculated for both terminations; Δz_k is the cation-oxygen off-centering at each monolayer k, and ΔP_k the associated electric polarization, as a function of the relative cation position (z_k/a_0) on each layer. A crucial difference emerges in the polarization of the two terminations: The signs of ΔP_k associated with TiO$_2$ layers (blue diamonds in Fig. 1) are positive for SrO termination and negative for TiO$_2$ termination, i.e., the Ti-O$_2$ dipoles have opposite directions, pointing outward for SrO and inward for TiO$_2$. This difference was noticed in a previous work [12], but since the era of 2DEG in STO was yet to start, no particular attention was paid to the consequence that this could have in terms of electron confinement, illustrated in the sketches of Fig. 1(a): For the SrO surface, the Ti-O dipoles are oriented outward (positive rumpling), and the associated electrostatic potential felt by the electrons favors electron accumulation to the right (i.e., to the surface); for the TiO$_2$ termination, the Ti-O dipoles are oriented inward (negative rumpling), thus the electrostatic potential pushes electron to the left, i.e., towards the substrate and away from the surface. This cartoon is indeed reproduced by the actually calculated macroscopic-averaged electrostatic potential (described in Sec. II), shown in Figs. 1(a$_3$) and 1(b$_3$). The macroscopic average usefully sets apart the periodic,

TABLE I. Atomic displacements along z, as a percentage of the lattice constant a_0, calculated for both terminations, for the first four monolayers, i.e., the first two perovskite units (layer 1 is the surface layer). Negative and positive signs indicate inward and outward displacement, respectively. Δd_{12} is the relative interlayer distance between surface and subsurface layer, as a percentage of a_0 (positive and negative values indicate stretching and contraction, respectively). S is the cation-oxygen off-plane displacement (rumpling) at the surface layer, as a percentage of a_0 (a negative S indicates a cation-oxygen dipole oriented towards the substrate, i.e., a relative oxygen shift towards the vacuum).

Layer	SrO term		Layer	TiO_2 term	
1 Sr,O	− 6.4	1.8	1 Ti,O	− 5.4	0.7
2 Ti,O	2.4	0.45	2 Sr,O	4.5	− 0.5
3 Sr,O	− 0.9	0.5	2 Ti,O	− 0.8	0.2
4 Ti,O	0.6	0.2	2 Sr,O	0.6	− 0.1
	Δd_{12}	S		Δd_{12}	S
	− 4.9	− 4.3		− 4.3	− 3.2

bulklike region of constant potential (conventionally set to zero) from the surface region where the potential deviates from constancy. For the TiO_2 termination the potential rises dramatically, with some oscillations, when moving from bulk to surface. On the contrary, the SrO termination exhibits an evident negative, i.e., electron-confining, effective potential over the two outer TiO_2 layers, between the bulklike constant potential, on the left, and the steep ascent of the potential heading to vacuum level [the work function of STO (001) is about 4.1 eV] on the right. This binding potential step is about 0.12 eV deep, and the local slope $\sim 3\times10^6$ V/cm.

Finally, it is interesting to compare these results with the rumpling observed at the STO/LAO interface. For the insulating interface (i.e., for LAO thickness lower than 4 u.c.) the measured rumpling is remarkable (2%–4%) [56,57], albeit somewhat smaller than for the surface; furthermore, in the LAO side rumpling is positive and counteracts the electrostatic potential rise due to the polarity of the film (as clearly shown in Fig. 3 of Ref. [56]); in the STO side rumpling is negative, thus it plays against the charge confinement at the interface (indeed, it is well known that at clamped ions the electron gas in STO/LAO is much more tightly confined than after relaxations). Thus, we have two very different situations: At the nonpolar (001) STO surface the rumpling is the only source of charge polarization, and plays a major role in the charge-confinement mechanism; at variance, in STO/LAO the rumpling is a secondary effect with respect to the LAO polarity, and plays against the electrostatic bending responsible of the 2D confinement.

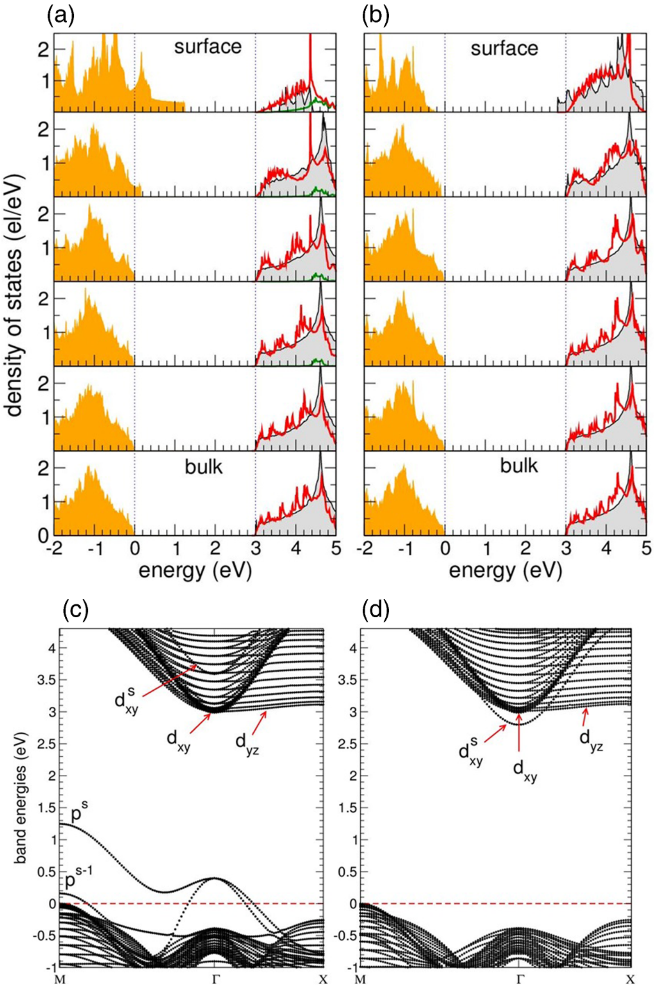

FIG. 2. (Color online) (a) Layer- and orbital-resolved DOS calculated for the (001) STO surface with TiO_2 termination. (b) Same property for the SrO-terminated surface. Only the relevant orbital contributions are shown: O p (solid orange); Ti 3d d_{xy} (solid gray); d_{xz}, d_{yz} (red); d_{z^2} (green). The uppermost panels show the DOS of the surface layers, the lowest panels the DOS of the most bulklike; zero is set at the VBT of the inmost bulklike layers. The dotted vertical lines in correspondence of VBT and CBB bulk values help to visualize the band bending due to the surface dipoles. (c) Band structure for the TiO_2-terminated surface; $M=[\pi/a_0,\ \pi/a_0,\ 0]$, $X=[\pi/a_0,\ 0,\ 0]$. The red dashed line indicates the bulk VBT taken as the energy zero. The orbital character of the most important bands is indicated. (d) Band structure for the SrO-terminated surface.

B. Electronic properties of the insulating surface

The different electrostatics of the two terminations, electron-confining for the SrO and electron-repulsive for the TiO_2 also reverberates in their radically different electronic properties. At the surface, much the same as at the STO/LAO interface, the Ti 3d t_{2g} states which form the conduction band bottom (CBB) split in a d_{xy} singlet and a (d_{xz}, d_{yz}) doublet. By its very chemical nature, the former lies purely within the plane, and as such it is highly sensitive to the bending of the potential profile along z. The (d_{xz}, d_{yz}) states, on the other hand, are fairly localized in a single planar direction but dispersed along z, then less sensitive to the electrostatic bending, and more reflective of their bulk shape. These features are well visible in the electronic properties shown in Fig. 2. In Figs. 2(a) and 2(b) the density of states (DOS) of both terminations is decomposed in different layer and orbital contributions. For clarity, only the important orbitals are reported [the O p states which dominate the valence band top (VBT) and the Ti 3d orbitals which form the CBB]. Each panel refers to a different STO layer, from the most bulklike at the bottom to the outmost at the top. For both terminations the

TABLE II. Calculated band disalignment for both surface terminations. $\Delta\epsilon_{xy}$ is the d_{xy} band bottom energy of the outmost Ti layer with respect to the bulk CBB; $\Delta\epsilon_{xz} = \Delta\epsilon_{yz}$, same quantities for symmetry-equivalent d_{xz}, d_{yz} states; $\Delta t_{2g} = \epsilon_{xy} - \epsilon_{xz}$ (or $\epsilon_{xy} - \epsilon_{yz}$) is the on-site splitting at the outmost Ti site; Δp^s, Δp^{s-1}, top energy of O $2p$ surface bands located at the surface (s) and subsurface (s-1) STO layer, calculated with respect to the bulk VBT.

Surface	$\Delta\epsilon_{xy}$(eV)	$\Delta\epsilon_{xz}$, $\Delta\epsilon_{yz}$(eV)	Δt_{2g}(eV)	Δp^s(eV)	Δp^{s-1}(eV)
TiO_2	0.622	0.010	− 0.52	1.248	0.160
SrO	− 0.188	0.028	0.216	− 0.20	0

surface effects are very short ranged and substantially limited to the two outermost STO cells,

First consider the VBT profile across the panels, highlighted by dotted lines in Figs. 2(a) and 2(b), which essentially follows the electrostatic potential shape: For the TiO_2 termination, the DOS edge in the surface and subsurface TiO_2 layer is 1.2 and 0.2 eV higher than the bulk level (fixed at zero energy), respectively. In the corresponding band structure [Fig. 2(c)] we can recognize the bands which give rise to these shifted DOS's, being well separated by the valence bulk manifold. For the SrO termination, on the other hand, the VBT of the surface and subsurface TiO_2 layer is just 0.2 and 0.1 eV lower than the bulk VBT, respectively, thus no surface states are distinguishable in the valence band structure [Fig. 3(d)] which thus maintains a bulklike character. Moving to analyze the CBB profile, we see that for the TiO_2 termination the d_{xy} DOS of the outmost Ti layer is pushed ~0.6 eV above the CBB bulk level, while the (d_{xz}, d_{yz}) DOS are nearly aligned, from bulk to surface. On the contrary, the SrO termination shows a d_{xy} DOS bottom on the outmost Ti layer lowered by about 0.2 eV with respect to the CBB bulk level. A summary of the DOS disalignment for the two terminations is reported in Table II.

We thus face radically different situations for the two terminations. SrO presents a short-range band bending favorable to the electron confinement at the surface. This bending is an intrinsic property of the clean, insulating surface. Due to its bi-dimensional nature, the d_{xy} state belonging to the TiO_2 layer closest to the surface, thus most sensitive to this effect, is downshifted in energy by about 200 meV with respect to the analogous states of the inner TiO_2 layers. It follows that any electron charge that were to be injected into the system will start filling, first and foremost, this d_{xy} surface band. Owning to its highly anisotropic masses ($m^*_{xy} = (0.7,0.7,8.8)m_e$ according to our *ab initio* results and in agreement with the value reported in Ref. [1]) this DOS profile naturally leads to the formation of surface-confined 2DEG. A close analogy with 2DEG present at the STO/LAO interface descends from a similar $3d$ band splitting causing the confinement on the STO side of the junction, and from the misalignment between $3d$ bands and vacuum level, which is analogous to the huge offset between (Ti d and Al s) conduction bands acting as a confining barrier on the LAO side of the STO/LAO interface. At the TiO_2-terminated surface, on the other hand, d electrons experiment a strong electrostatic repulsion pushing the d_{xy} states of the outmost Ti layer ~0.6 eV above the bulk CBB, thus preventing the formation of surface-confined 2DEG. In the absence of any confining potential, the electron charge provided by the doping or field effect will not be collected at the surface, but redistributed within the bulk, simply changing the 3D conductivity.

C. Evolution of the electronic properties with carrier density

It was put in evidence in previous calculations and experiments [18,19] that the electronic structure in oxide-based 2DEG systems may be crucially dependent on the amount of confined charge. In particular, in STO/LAO the charge concentration controls the on-site splitting (Δt_{2g}) between lower-energy d_{xy} and higher-energy (d_{xz}, d_{yz}) states responsible for the 2D confinement and, in turn, the localization length: at small concentration (Hall experiments typically report n_{2D} ~3–6 $\times 10^{13}$ cm^{-2}) Δt_{2g} is only a few tenths of meV (for $n_{2D} = 0 \quad \Delta t_{2g} = 28$ meV); then it increases smoothly with the charge up to $\Delta t_{2g} \simeq 350$ meV for the half-electron per unit area ($n_{2D} \simeq 3.2\times 10^{14}$ cm^{-2}) predicted by the polarization catastrophe model. On the other hand, for the SrO surface Δt_{2g} is already quite large (216 meV) for the insulating surface, i.e., in the absence of mobile charge. This is an important difference between the STO/LAO and STO surfaces in terms of the evolution of the electronic structure with charge concentration.

For the surface we considered two charge doping levels (the related methodology is described in Sec. II) corresponding to 0.08 electrons per unit area ($n_{2D} = 5.3\times 10^{13}$ cm^{-2}) and 0.1 electrons per unit area ($n_{2D} = 6.6\times 10^{13}$ cm^{-2}). The atomic structures change only marginally with the added charge (about 5% in rumpling) since the added charge is small, and the STO polarizability is largely reduced by the atomic relaxations of the surface. In Fig. 3 a closeup of the DOS in a small energy interval near the CBB is shown for the insulating surface, and for two different doping concentrations. For the SrO termination [Figs. 3(a)–3(c)] the DOS profile remains roughly similar even in the presence of charge, with the bottom of the surface DOS lying ~0.2 eV below E_F; in particular, for $n_{2D} = 5.3\times 10^{13}$ cm^{-2} [Fig. 3(b)]E_F lies right at the bottom of the bulklike DOS, thus this charge density corresponds to the highest density which can be fully confined in the sole surface layer. For a further increase of carrier concentrations [$n_{2D} = 6.6\times 10^{13}$ cm^{-2}, Fig. 3(c)] the additional charge spreads uniformly through the cell, thus causing an almost rigid upward shift of E_F above the bulklike bottom DOS. In words, the picture drawn for the SrO termination is that of a strong band bending at the surface which confines a fairly large amount of doping charge (6×10^{13} electrons per cm^2) within an almost rigid (i.e., charge-independent) electrostatic well; a further increase of carrier concentration above this maximum 2DEG threshold causes the charge to spread into the substrate, eventually giving rise to some 3D conductivity, but only weakly affecting the electronic structure at the surface and the corresponding ARPES spectra. In this sense, we can describe the 2DEG behavior as "universal," i.e., substantially independent (or weakly dependent) on the overall doping concentration of the sample. However, this universality is not quantitatively exact since, at varying doping, small fluctuation in atomic relaxations, electric dipoles, and electrostatic bending, cause visible differences in the band

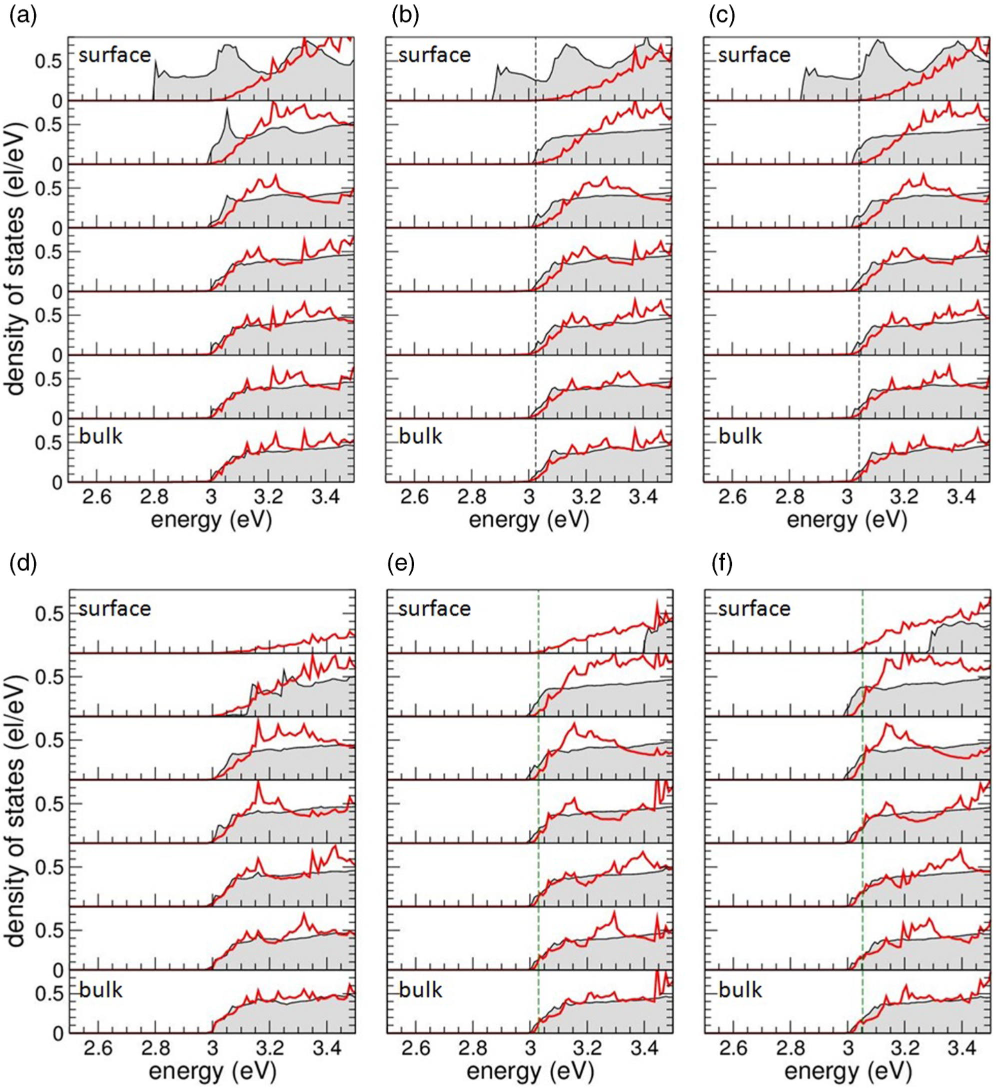

FIG. 3. (Color online) (a)–(c) Layer-by-layer DOS for the SrO-terminated surface for different doping densities. The energy zero is fixed at the bulk VBT. (a) Undoped surface; (b) surface with 0.08 electrons per unit area ($n_{2D} = 5.3\times10^{13}$ cm^{-2}); (c) surface with 0.1 electrons per unit area ($n_{2D} = 6.6\times10^{13}$ cm^{-2}). Only Ti 3d d_{xy} (solid gray) and d_{xz}, d_{yz} (red) orbitals are shown in a small energy interval around the CBB. Dashed vertical lines indicate E_F. (d)–(f) Layer-by-layer DOS for the TiO$_2$-terminated surface at varying charge density. Labels and doping charges are the same as in (a)–(c), respectively.

disalignment (see in Table III the band bottom energy E_b calculated with respect to E_F at varying doping). Our calculated sheet density threshold is in good agreement with the 2DEG density $n_{2D} = 8\times10^{13}$ cm^{-2} reported in Ref. [2], but smaller than the value $n_{2D} = 2\times10^{14}$ cm^{-2} estimated by Fermi surface areas in Ref. [1], due to the presence of more bands in the ARPES spectra of the latter, which will be analyzed below. In the case of the TiO$_2$ termination, on the other hand, it is very clear that no charge accumulation at the surface occurs, at any doping. Thus for this surface a sheet density n_{2D} cannot be properly defined, and the progressive increase of mobile charge has the effect to rise nearly rigidly E_F above the DOS bottom,

TABLE III. Fermi energies (E_F) and lowest band bottom energy (E_b) for both terminations and three different doping levels; n_{3D} and n_{2D} are charge densities in 3D and 2D; n_{2D} is properly defined only for SrO since no 2DEG is formed on TiO$_2$. E_F is calculated with respect to the bulk VBT; for the undoped case E_F is the bulk CBB, thus it corresponds to the bulk energy band gap. E_b is calculated with respect to E_F.

		SrO			TiO$_2$	
n_{3D} (10^{20} el/cm^3)	0	1.85	2.31	0	1.85	2.31
n_{2D} (10^{13} el/cm^2)	0	5.35	6.70	0	5.35	6.70
E_F (eV)	2.986	3.024	3.043	2.986	3.030	3.052
E_b (eV)	− 0.188	− 0.147	− 0.205	0	− 0.037	− 0.064

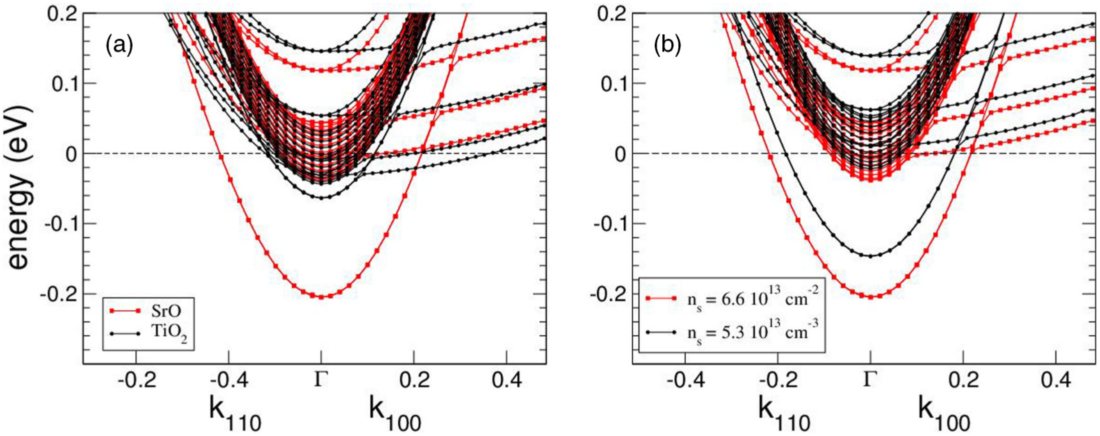

FIG. 4. (Color online) (a) Juxtaposed band structures for SrO (red squares) and TiO$_2$ (black circles) terminations, calculated for $n_s = 6.6\times10^{13}$ cm^{-3} doping charge. E_F of both systems is shifted to zero. (b) Band structure for SrO termination at two different doping values. Black dashed lines indicate E_F. K_{100} and K_{110} indicate k-point strings along $\Gamma - X$ and $\Gamma - M$ directions, respectively; k values are in units of $\pi/a_0 = 0.813$ Å^{-1}.

giving rise to 3D conductivity. In this situation, ARPES signals could be eventually interpreted as due to bulklike electronic states spreading up to the surface layer.

In Fig. 4(a) we report the calculated bands of a 50%–50% superposition of the two terminations at $n_{2D} = 6.6\times10^{13}$ cm^{-2}, which should give an adequate representation of the vacuum-cleaved STO surfaces considered in Refs. [1] and [2]. ARPES-unresolved superposition of features from different terminations was previously reported in several cases of as-cleaved surfaces (see, e.g., Bi4Se3 [58] or BiTeI [59]). To that aim, two situations should occur: First, the as-cleaved surface must be terraced with both terminations exposing to the vacuum a substantially similar surface area. This in turn requires that the two terminations have a similar formation energy, as in the case of the STO (001). Second, the terrace size must be smaller than the light spot size, in order of not being resolved by the probe. In Fig. 4(b) we report the band structure juxtaposition of two different doping levels for the same SrO termination. These bands should capture a situation in which the surface is affected by doping inhomogeneities on a macroscopic scale; the resulting ARPES may then be interpreted as a weighted superposition of two, differently doped regimes.

It is now useful to compare quantitatively our results with ARPES. The most 2D-like band, i.e., the d_{xy} surface band calculated for the SrO termination, is unambiguously revealed in all the experiments, for both vacuum-cleaved [1,2] and even TiO$_2$-etched surfaces [3,4] (we will comment at the end of the section on this apparent contrast with the calculations). The dominant and energy-lowest signal is always associated with a dispersed band with small mass ($m^\star \sim 0.7\, m_e$) spreading in both k_x and k_y, with clear d_{xy} orbital character. Also, the different experiments estimate very similar values for the band bottom ($E_b = 210$, 216, and 230 meV according to Refs. [1], respectively) and Fermi vector ($k_F = 0.21$ Å^{-1}, 0.175 Å^{-1}, and ~0.16 Å^{-1}, respectively), also in good agreement with our values of E_b (see Table III) and k_F (0.16 Å^{-1} and 0.176 Å^{-1} for $n_{2D} = 5.3\times10^{13}$ cm^{-2} and 6.6×10^{13} cm^{-2}, respectively).

As to the other features visualized by ARPES, the interpretation is less straightforward. In Ref. [2] a second d_{xy} state is seen, slightly shallower (E_b=110 meV, $k_F = 0.12$ Å^{-1}) than the previous one. This state also appears, with very similar characteristics, in the spectra of Refs. [3] and [4], both concerning etched TiO$_2$ termination. A simple interpretation on the basis of our results is that this signal could be the tip of the bulklike d_{xy} band manifold dipping below E_F for both the terminations [see Fig. 4(a)]. However, the analysis of the k_z dispersion in Ref. [2] indicates that it is probably a genuine surface state. In fact, a plausible interpretation based on spin-resolved ARPES spectra [4] is that the two d_{xy} states are the result of the spin-orbit Rashba splitting, and as such, absent in our spin-degenerate description.

In Ref. [1] three additional signals are present, two of them attributed to the d_{xz} and d_{yz} states, plus a flat state crossing the whole Brillouin zone (BZ) (thus completely filled, to be attributed to localized defects). In Ref. [2], on the other hand, d_{xz} and d_{yz} states do not appear. They appear instead in Ref. [3], where different photon energies are used to probe the states at different k_z planes. Interestingly, it is found that these states are flattened along the surface-orthogonal direction in the form of flying saucers, with quite large effective mass m_z^*=15 m$_e$. According to our results, these d_{xz} and d_{yz} states should be primarily related to the TiO$_2$ termination, and interpreted more as projected 3D states, rather than as surface-localized states, in agreement with the interpretation given in Ref. [3]. In our supercell calculations the band dispersion along z cannot be easily determined, however, our values of E_b (−30 meV) and k_F (0.3 Å^{-1}) for the d_{xz}, d_{yz} states [see Fig. 4(a)] are close to those reported in Ref. [1].

In summary, most of the qualitative and even quantitative characteristics of our calculated band structures apparently match well the features revealed in the ARPES spectra; however, an evident discrepancy stems from the fact that the d_{xy} surface states should, according to our calculations, be only present at the SrO termination, while these are clearly revealed in chemically etched TiO$_2$ surfaces as well. The most obvious rationale is that at the real surface, additional extrinsic factors, not captured by our simulations, can be juxtaposed to the purely intrinsic behavior and play a role in the creation of electron gas. Clearly the accumulation of oxygen vacancies at the surface can act as the confining potential [1]; the lengthy exposure to ultraviolet irradiation can further modify 2DEG by extending the region of gas confinement [3]. And yet, it is quite remarkable that despite the differences in experimental settings and sample conditions, the major characteristics of the gas revealed by the ARPES are closely reproduced by our "ideal" calculations. Stated differently, our calculations show that the "universal" behavior which characterizes this 2DEG is sufficiently captured even in the limit of a purely intrinsic description.

D. Transport properties

We used the calculated band structure as input for the Bloch-Boltzmann theory [26] to determine, in the diffusive regime, the transport properties of 2DEG at the STO surface, as a function of temperature and doping. The scattering rates, modeled in a simple analytic form including temperature and energy dependencies (see details in Methods section) account for impurity scattering, acoustic phonon scattering, and polar-optical phonon scattering. Scattering model parameters are those for STO bulk, thus with no ad hoc adjustment for the surface.

In Fig. 5 results for electric resistivity, Hall resistivity, and mobility are reported at various doping concentrations. Transport properties resemble those found in STO/LAO. Above $T = 50$ K, they are dominated by optical polar phonon scattering; resistivity increases as $T^{2.8}$ in the range 50–100 K, T^2 above 100 K. At low temperature, on the other hand, acoustic phonon scattering takes place, with a $\sim T$ behavior. The mobility decreases accordingly as T^{-2} above 100 K, $T^{-2.8}$ between 50 and 100 K, and $\sim T^{-1}$ below 50 K.

While qualitatively similar, there are quantitative differences between the two terminations: At high temperature, the SrO termination is more metallic, i.e., has lower resistivity and higher mobility (e.g., at T=300 K for $n_{3D} = 10^{18}$ cm^{-3} we obtain $\rho = 1.03\ \Omega$ cm, $\mu = 6.07$ cm^2/Vs in SrO, against $\rho = 1.64\ \Omega$ cm, $\mu = 3.80$ cm^2/Vs in TiO$_2$); at low T the situation is reversed, and the resistivity (mobility) is higher (lower) for the SrO termination. The rationale of this behavior resides in the different metallic character: For the SrO termination the mobile charge is 2DEG mostly confined within the surface layer, while for the TiO$_2$ termination it is homogeneously diluted through the substrate, thus resembling a 3D metal or degenerate semiconductor. Thus the "effective" 3D density $n_{\text{eff}} = Q/A\,d$ (where Q is the total charge, A the unit surface area, and d the layer thickness over which the charge actually spreads) is much larger for the SrO termination. At high temperature, where optical polar phonon scattering dominates, the relaxation time $\tau \simeq (\epsilon - \epsilon_{\text{CBB}})^{3/2}$ strongly increases with the energy of the carrier, so that density accumulation favors higher mobility. At low temperature, on the other hand, the relaxation time associated with acoustic phonon scattering is $\tau \simeq (\epsilon - \epsilon_{\text{CBB}})^{-1/2}$, so that lower energy means weaker scattering; it follows that charge dilution favors higher mobility.

Finally, the calculated inverse Hall resistivity matches quite well the nominal charge concentration across the whole temperature range, with minor deviations only visible at low temperature. Since $R_H = -r_H/en_{3D}$, where $r_H = \langle\tau^2\rangle/\langle\tau\rangle^2$ is the Hall factor ($\langle\tau^2\rangle$ and $\langle\tau\rangle$ being the average over energy of τ^2 and τ), we argue that the Hall factor is close to unity, and the Hall mobility coincides with the electric mobility.

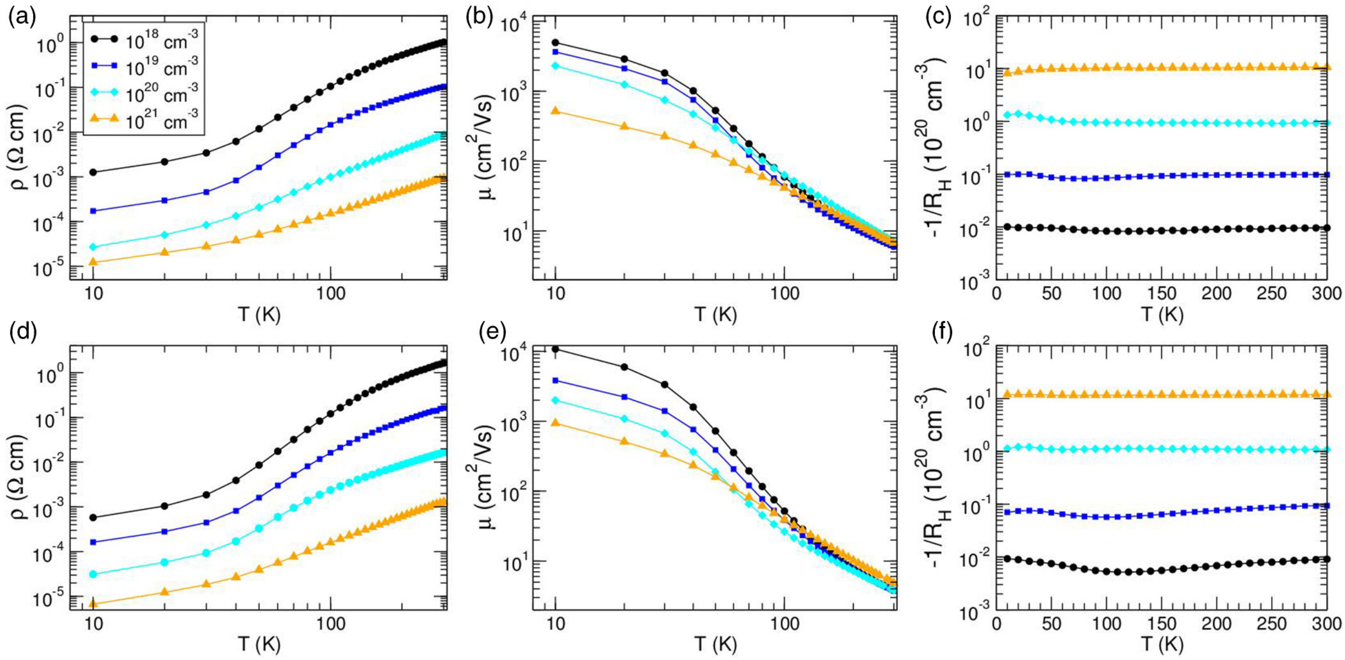

FIG. 5. (Color online) Calculated electric resistivity, mobility, and inverse Hall resistivity transport properties for SrO-terminated (a)–(c) and TiO$_2$-terminated (d)–(f) STO surface. Different colors are for different n-type doping levels [indicated in the legend of (a)]. (a) Resistivity; (b) mobility; (c) inverse Hall resistivity.

TABLE IV. Calculated in-plane dc resistivity ρ, inverse Hall resistivity $-e/R_H$, and mobility μ at $T = 295$ K for two doping concentrations n_{3D} matching those measured at the same temperature by Hall in Ref. [1] (in parentheses the experimental values). The measured mobility is actually the Hall mobility, which, however, should be similar to the electric mobility, as discussed in the text.

	SrO			TiO$_2$		
n_{3D}(cm^{-3})	ρ(Ω (cm)	$-e/R_H$ (cm^{-3})	μ (cm^2/Vs)	ρ(Ω cm)	$-e/R_H$ (cm^{-3})	μ (cm^2/Vs)
3.3×10^{18}	0.30 (0.29)	3.2×10^{18}	6.15 (7)	0.49	3.0×10^{18}	3.92
7.7×10^{19}	0.012 (0.011)	7.2×10^{19}	7.16 (7.1)	0.021	8.2×10^{19}	3.88

As a validation of the results, in Table IV we report values calculated at $T = 295$ K for two 3D doping concentrations matching those measured in Ref. [1]. Notice that the Hall-measured densities are lower than the 2DEG threshold of the SrO termination; thus, the contribution to transport from this termination should entirely come from the 2DEG confined at the surface layer. We see that the agreement is surprisingly good when compared to the SrO termination. This result seems to suggest that transport and Hall measurements mainly probe the surface charge present at the SrO termination. From the methodological viewpoint, this agreement also indicates that the scattering model parameters appropriate for bulk STO are valid for the STO surface as well.

IV. CONCLUSIONS

In this work we studied by advanced *ab initio* calculations structural, electronic, and transport properties of the unreconstructed (001) STO surface, which represents one of the very few proved cases of 2DEG systems in oxide heterostructures. The major result of our analysis is that 2DEG can originate even from purely intrinsic surface properties. The intrinsic confinement mechanism is only active at the SrO termination, and derives from the large electric polarization induced by atomic relaxations at the surface. The resulting surface potential well, as deep as 0.2 eV, confines conduction electrons solely in the TiO$_2$ layer closer to the surface, and with a maximum density as large as $n_{2D} = 6 \times 10^{13}$ cm^{-2}. On the other hand, the surface polarization at the TiO$_2$ termination is oppositely oriented to that of the SrO termination, and (in absence of any additional extrinsic mechanism) repels the conduction charge away from the surface. Since 2DEG is actually observed both at vacuum-cleaved surfaces (including an even mixture of both terminations) and in chemically etched TiO$_2$ termination, we may argue that for the latter 2DEG should be exclusively derived by extrinsic mechanisms, namely oxygen vacancies and/or UHV irradiation, while for the former both intrinsic and extrinsic ingredients may eventually cooperate to create 2DEG.

The quantitative comparison of our results with ARPES spectra is rather satisfying, insofar as most of the important spectral features are well reproduced by our band structure for sheet densities in the range of the observed values (i.e., $n_{2D} \sim 5\text{–}8 \times 10^{13}$ cm^{-2}). This agreement, somewhat surprising considering the variety of sample preparations and experimental conditions, is the fingerprint of the well-documented "universal" character of 2DEG, whose characteristics are largely independent (or weakly dependent) not only on the doping concentration but even on the fundamental mechanism which drives the gas formation.

From an operative viewpoint, our results represent a stimulus to look with more interest at the SrO termination, while so far the vast majority of studies has focused on the TiO$_2$ termination. The prominence of the TiO$_2$ termination was historically motivated by the possibility to obtain, starting from an as-received vacuum-cleaved sample, a flat and nearly complete TiO$_2$ termination through an efficient wet-etching procedure, first introduced in Ref. [60] and later refined over the years by a number of studies [61–67]. Later on, the 2DEG discovery at the STO/LAO interface further ignited the rush towards the realization of better and better single-terminated TiO$_2$ substrates. On the other hand, obtaining a pure SrO termination is more complicated (usually one SrO layer is deposited on a wet-etched TiO$_2$ termination [68]) and the resulting surface is typically affected by larger roughness than TiO$_2$. However, recent works demonstrated that high-quality, stable SrO termination can be obtained by growing STO onto a diagnostic substrate [69], thus opening an possible route for the exploitation of this termination.

ACKNOWLEDGMENTS

We acknowledge partial support from the Italian Ministry of University and Research (MIUR) under Progetti di Rilevante Interesse Nazionale (PRIN) 2010, project Oxide; Fondazione Banco di Sardegna through research grants; CINECA grants; the Centro Ricerche e Studi Superiori in Sardegna (CRS4) computing facility; and the CAR fund of University of Cagliari. P.D. thanks the Istituto Italiano di Tecnologia for financial support.

[1] A. F. Santander-Syro, O. Copie, T. Kondo, F. Fortuna, S. Pailhes, R. Weht, X. G. Qiu, F. Bertran, A. Nicolaou, A. Taleb-Ibrahimi, P. Le Fevre, G. Herranz, M. Bibes, N. Reyren, Y. Apertet, P. Lecoeur, A. Barthelemy, and M. J. Rozenberg, Nature (London) **469**, 189 (2011).

[2] W. Meevasana, P. D. C. King, R. H. He, S.-K. Mo, M. Hashimoto, A. Tamai, P. Songsiriritthigul, F. Baumberger, and Z.-X. Shen, Nat. Mater. **10**, 114 (2011).

[3] N. C. Plumb, M. Salluzzo, E. Razzoli, M. Månsson, M. Falub, J. Krempasky, C. E. Matt, J. Chang, M. Schulte, J. Braun,

H. Ebert, J. Minár, B. Delley, K.-J. Zhou, T. Schmitt, M. Shi, J. Mesot, L. Patthey, and M. Radovi, Phys. Rev. Lett. **113**, 086801 (2014).

[4] A. F. Santander-Syro, F. Fortuna, C. Bareille, T. C. Rödel, G. Landolt, N. C. Plumb, J. H. Dil, and M. Radović, Nat. Mater. **13**, 1085 (2014).

[5] P. D. C. King, S. McKeown Walker, A. Tamai, A. de la Torre, T. Eknapakul, P. Buaphet, S.-K. Mo, W. Meevasana, M. S. Bahramy, and F. Baumberger, Nat. Commun. **5**, 3414 (2014).

[6] C. Rodenbucher, S. Wicklein, R. Waser, and K. Szot, Appl. Phys. Lett. **102**, 101603 (2013).

[7] M. DAngelo, R. Yukawa, K. Ozawa, S. Yamamoto, T. Hirahara, S. Hasegawa, M. G. Silly, F. Sirotti, and I. Matsuda, Phys. Rev. Lett. **108**, 116802 (2012).

[8] J. Delahaye and T. Grenet, J. Phys. D: Appl. Phys. **45**, 315301 (2012).

[9] A. B. Eyvazov, I. H. Inoue, P. Stoliar, M. J. Rozenberg, and C. Panagopoulos, Sci. Rep. **3**, 1721 (2013).

[10] R. Di Capua, M. Radovic, G. M. De Luca, I. Maggio-Aprile, F. Miletto Granozio, N. C. Plumb, Z. Ristic, U. Scotti di Uccio, R. Vaglio, and M. Salluzzo, Phys. Rev. B **86**, 155425 (2012).

[11] J. Padilla and D. Vanderbilt, Surf. Sci. **418**, 64 (1998).

[12] E. Heifets, E. Kotomin, and J. Maier, Surf. Sci. **462**, 19 (2000).

[13] N. Bickel, G. Schmidt, K. Heinz, and K. Müller, Phys. Rev. Lett. **62**, 2009 (1989).

[14] M. Kawasaki, A. Ohtomo, T. Arakane, K. Takahashi, M. Yoshimoto, and H. Koinuma, Appl. Surf. Sci. **107**, 102 (1996).

[15] G. Koster, G. Rijnders, D. H. Blank, and H. Rogalla, Physica C: Superconductivity **339**, 215 (2000).

[16] Y. J. Chang, A. Bostwick, Y. S. Kim, K. Horn, and E. Rotenberg, Phys. Rev. B **81**, 235109 (2010).

[17] A. Filippetti, C. D. Pemmaraju, S. Sanvito, P. Delugas, D. Puggioni, and V. Fiorentini, Phys. Rev. B: Condens. Matter Mater. Phys. **84**, 195127 (2011).

[18] P. Delugas, A. Filippetti, V. Fiorentini, D. I. Bilc, D. Fontaine, and P. Ghosez, Phys. Rev. Lett. **106**, 166807 (2011).

[19] C. Cancellieri, M. L. Reinle-Schmitt, M. Kobayashi, V. N. Strocov, P. R. Willmott, D. Fontaine, P. Ghosez, A. Filippetti, P. Delugas, and V. Fiorentini, Phys. Rev. B **89**, 121412 (2014).

[20] A. Filippetti, P. Delugas, M. J. Verstraete, I. Pallecchi, A. Gadaleta, D. Marré, D. F. Li, S. Gariglio, and V. Fiorentini, Phys. Rev. B **86**, 195301 (2012).

[21] P. Delugas, A. Filippetti, M. J. Verstraete, I. Pallecchi, D. Marré, and V. Fiorentini, Phys. Rev. B **88**, 045310 (2013).

[22] P. Delugas, A. Filippetti, A. Gadaleta, I. Pallecchi, D. Marré, and V. Fiorentini, Phys. Rev. B **88**, 115304 (2013).

[23] D. Puggioni, A. Filippetti, and V. Fiorentini, Phys. Rev. B **86**, 195132 (2012).

[24] A. Baldereschi, S. Baroni, and R. Resta, Phys. Rev. Lett. **61**, 734 (1988).

[25] L. Colombo, R. Resta, and S. Baroni, Phys. Rev. B **44**, 5572 (1991).

[26] P. Allen, in *Quantum Theory of Real Materials*, edited by J. R. Chelikowsky and S. G. Louie (Kluwers, Boston, 1996), pp. 219–250.

[27] G. K. Madsen and D. J. Singh, Comput. Phys. Commun. **175**, 67 (2006).

[28] B. K. Ridley, J. Phys.: Condens. Matter **10**, 6717 (1998).

[29] D. R. Anderson, N. A. Zakhleniuk, M. Babiker, B. K. Ridley, and C. R. Bennett, Phys. Rev. B **63**, 245313 (2001).

[30] J. T. Devreese, S. N. Klimin, J. L. M. van Mechelen, and D. van der Marel, Phys. Rev. B **81**, 125119 (2010).

[31] N. Erdman, K. R. Poeppelmeier, M. Asta, O. Warschkow, D. E. Ellis, and L. D. Marks, Nature (London) **419**, 55 (2002).

[32] M. R. Castell, Surf. Sci. **505**, 1 (2002).

[33] T. Kubo and H. Nozoye, Surf. Sci. **542**, 177 (2003).

[34] R. Herger, P. R. Willmott, O. Bunk, C. M. Schlepütz, B. D. Patterson, and B. Delley, Phys. Rev. Lett. **98**, 076102 (2007).

[35] R. Herger, P. R. Willmott, O. Bunk, C. M. Schlepütz, B. D. Patterson, B. Delley, V. L. Shneerson, P. F. Lyman, and D. K. Saldin, Phys. Rev. B **76**, 195435 (2007).

[36] D. M. Kienzle and L. D. Marks, Cryst. Eng. Comm. **14**, 7833 (2012).

[37] Y. Lin, A. E. Becerra-Toledo, F. Silly, K. R. Poeppelmeier, M. R. Castell, and L. D. Marks, Surf. Sci. **605**, L51 (2011).

[38] R. Shimizu, K. Iwaya, T. Ohsawa, S. Shiraki, T. Hasegawa, T. Hashizume, and T. Hitosugi, Appl. Phys. Lett. **100**, 263106 (2012).

[39] V. Vonk, S. Konings, G. van Hummel, S. Harkema, and H. Graafsma, Surf. Sci. **595**, 183 (2005).

[40] G. Charlton, S. Brennan, C. Muryn, R. McGrath, D. Norman, T. Turner, and G. Thornton, Surf. Sci. **457**, L376 (2000).

[41] A. Kazimirov, D. Goodner, M. Bedzyk, J. Bai, and C. Hubbard, Surf. Sci. **492**, L711 (2001).

[42] A. Fragneto, G. M. De Luca, R. Di Capua, U. Scotti di Uccio, M. Salluzzo, X. Torrelles, T.-L. Lee, and J. Zegenhagen, Appl. Phys. Lett. **91**, 101910 (2007).

[43] T. Hikita, T. Hanada, M. Kudo, and M. Kawai, Surf. Sci. **287–288**, 377 (1993).

[44] M. Kudo, T. Hikita, T. Hanada, R. Sekine, and M. Kawai, Surf. Interf. Anal. **22**, 412 (1994).

[45] T. Nishimura, A. Ikeda, H. Namba, T. Morishita, and Y. Kido, Surf. Sci. **421**, 273 (1999).

[46] A. Ikeda, T. Nishimura, T. Morishita, and Y. Kido, Surf. Sci. **433–435**, 520 (1999).

[47] Y. Kido, T. Nishimura, Y. Hoshino, and H. Namba, Nucl. Instrum. Methods Phys. Res., Sect. B: Beam Interact. Mater. At. **161–163**, 371 (2000).

[48] E. A. Kotomin, R. I. Eglitis, J. Maier, and E. Heifets, Thin Solid Films **400**, 76 (2001).

[49] E. Heifets, R. I. Eglitis, E. A. Kotomin, J. Maier, and G. Borstel, Phys. Rev. B **64**, 235417 (2001).

[50] E. Heifets, R. Eglitis, E. Kotomin, J. Maier, and G. Borstel, Surf. Sci. **513**, 211 (2002).

[51] G. Borstel, R. I. Eglitis, E. A. Kotomin, and E. Heifets, J. Cryst. Growth **237**, 687 (2002).

[52] Z.-Q. Li, J.-L. Zhu, C. Q. Wu, Z. Tang, and Y. Kawazoe, Phys. Rev. B **58**, 8075 (1998).

[53] S. Piskunov, E. Kotomin, E. Heifets, J. Maier, R. Eglitis, and G. Borstel, Surf. Sci. **575**, 75 (2005).

[54] K. Johnston, M. R. Castell, A. T. Paxton, and M. W. Finnis, Phys. Rev. B **70**, 085415 (2004).

[55] V. Ravikumar, D. Wolf, and V. P. Dravid, Phys. Rev. Lett. **74**, 960 (1995).

[56] S. A. Pauli, S. J. Leake, B. B. Delley, M. Björck, C. W. Schneider, C. M. Schlepütz, D. Martoccia, S. Paetel, J. Mannhart, and P. R. Willmott, Phys. Rev. Lett. **106**, 036101 (2011).

[57] M. Salluzzo, S. Gariglio, X. Torrelles, Z. Ristic, R. Di Capua, J. Drnec, M. Moretti Sala, G. Ghiringhelli, R. Felici, and N. B. Brookes, Adv. Mater. **25**, 2333 (2012).

[58] Q. D. Gibson, L. M. Schoop, A. P. Weber, H. Ji, S. Nadj-Perge, I. K. Drozdov, H. Beidenkopf, J. T. Sadowski, A. Fedorov, A. Yazdani, T. Valla, and R. J. Cava, Phys. Rev. B **88**, 081108 (2013).

[59] G. Landolt, S. V. Eremeev, Y. M. Koroteev, B. Slomski, S. Muff, T. Neupert, M. Kobayashi, V. N. Strocov, T. Schmitt, Z. S. Aliev, M. B. Babanly, I. R. Amiraslanov, E. V. Chulkov, J. Osterwalder, and J. H. Dil, Phys. Rev. Lett. **109**, 116403 (2012).

[60] M. Kawasaki, K. Takahashi, T. Maeda, R. Tsuchiya, M. Shinohara, O. Ishiyama, T. Yonezawa, M. Yoshimoto, and H. Koinuma, Science **266**, 1540 (1994).

[61] G. Koster, B. L. Kropman, G. J. Rijnders, D. H. Blank, and H. Rogalla, Mater. Sci. Eng.: B **56**, 209 (1998).

[62] G. Koster, B. L. Kropman, G. J. H. M. Rijnders, D. H. A. Blank, and H. Rogalla, Appl. Phys. Lett. **73**, 2920 (1998).

[63] M. R. Castell, Surf. Sci. **516**, 33 (2002).

[64] M. Kareev, S. Prosandeev, J. Liu, C. Gan, A. Kareev, J. W. Freeland, M. Xiao, and J. Chakhalian, Appl. Phys. Lett. **93**, 061909 (2008).

[65] H. Moon, J. H. Cho, and J. S. Ahn, J. Kor. Phys. Soc. **47**, 251 (2005).

[66] J. G. Connell, B. J. Isaac, G. B. Ekanayake, D. R. Strachan, and S. S. A. Seo, Appl. Phys. Lett. **101**, 251607 (2012).

[67] I. Velasco-Davalos, R. Thomas, and A. Ruediger, Appl. Phys. Lett. **103**, 202905 (2013).

[68] A. Hirata, K. Saiki, A. Koma, and A. Ando, Surf. Sci. **319**, 267 (1994).

[69] M. Radovic, N. Lampis, F. M. Granozio, P. Perna, Z. Ristic, M. Salluzzo, C. M. Schleputz, and U. Scotti di Uccio, Appl. Phys. Lett. **94**, 022901 (2009).